Adsorption of Graphene to Metal (111) Surfaces using the Exchange-Hole Dipole Moment Model

Matthew S. Christian[a], A. Otero-de-la-Roza[b], Erin R. Johnson[a,*]

[a]*Department of Chemistry, Dalhousie University, 6274 Coburg Road, Halifax, Nova Scotia, Canada B3H 4R2*
[b]*Department of Chemistry, University of British Columbia, Okanagan, 3247 University Way, Kelowna, British Columbia, Canada V1V 1V7.*

Abstract

Graphene has a unique electronic structure and excellent tribological properties. A promising method for graphene production involves depositing vaporized carbon on metal substrates, which can also be used to modify graphene's electronic structure through charge transfer. In this work, graphene adsorption on the (111) surface of seven metals (Al, Cu, Ag, Au, Ni, Pd, and Pt) is investigated computationally using density-functional theory with the exchange-hole dipole moment (XDM) dispersion correction. Two distinct graphene-metal orientations, corresponding to 0° and 30° relative rotation of the graphene layer, are considered to investigate how lattice mismatch affects adsorption. Our results reproduce reference data from the random-phase approximation more closely than any other dispersion-corrected density functional, confirming that XDM is an excellent method for surface chemistry. The rotational orientation of graphene is found to strongly affect its interaction with the substrate. There is an energetic drive for graphene to align with the metal lattice, particularly for Pd and Pt, which causes the formation of multiple Moiré patterns, in agreement with experimental observations.

1. Introduction

Graphene is a material that holds the potential to revolutionize the semiconductor industry. Various applications have been proposed that utilize graphene's unique two-dimensional electronic structure [1–14]. Graphene has also been shown to be an excellent solid lubricant [14–16] that

*Corresponding author, E-mail: erin.johnson@dal.ca (Erin R. Johnson)

can reduce friction and wear in mechanical devices either through direct surface deposition or as an additive to petroleum-based lubricants [11, 17]. While the original scotch-tape method for graphene isolation [1] easily produces laboratory samples, it is not scalable for mass production. Lack of a suitable mass-production method has hindered commercialization of graphene-based technologies [6, 18], but several methods have showed promising results. One such method is chemical vapor deposition (CVD) [19–22], where a carbon feedstock is vaporized to produce pure carbon that is deposited on to a metal surface. Additionally, charge transfer from the underlying metal substrate [22] provides a mechanism to tune graphene's electronic structure through the alteration of its valence band [23].

Graphene-metal systems have been extensively investigated experimentally [18, 24–38] to understand electronic and tribological properties as well as monolayer growth mechanisms. These investigations have shown that graphene can either chemisorb, physisorb, or form a carbide phase on the surface [18, 24]. Metals on which graphene chemisorbs or physisorbs are of the most practical interest because the adsorbed graphene will retain its unique electronic structure.

The most promising substrates for graphene mass production are Cu and Ni. Not only are these metals inexpensive, but their surface lattice constant is close to that of graphene. This excellent lattice match results in a limited number of observed Moiré patterns and reliable formation of large continuous graphene monolayers on the surface [39–43]. In particular, a CVD method using Cu has shown promising results for graphene mass production [44]. Metals such as Pd [28–30], Pt [27, 31–36] and Au [26, 35, 37, 38] have also been investigated for graphene synthesis, but their lattice mismatch results in multiple Moiré patterns on single surface samples. Indeed, experiments suggest that there exist an infinite number of Moiré patterns for Pt and Pd [28, 30–33]. In the early stages of graphene patterning on Pd and Pt, local graphene domains will bind strongly to the surface, but as the monolayer size increases, the overall surface-substrate interaction weakens because of the lattice mismatch. Light emitting electron diffraction (LEED) experiments have shown that strong surface-substrate interactions occur on Pd and Pt but depend on the rotational alignment [29, 36], which has resulted in conflicting reports as to the nature of graphene-Pd/Pt interactions.

Many previous publications have used density-functional theory (DFT) to investigate graphene

adsorption on metal surfaces [42, 45–49]. Most studies employed the local density approximation (LDA) because it predicts reasonable chemisorption geometries [29, 32, 50–54]. However, the LDA is known to over-estimate chemisorption energies and under-estimate physisorption because it does not include the physics of London dispersion. This results in narrow potential energy surfaces (PES) at chemisorption distances, with only shallow binding at typical physisorption distances, in disagreement with higher levels of theory, such as the random-phase approximation (RPA) [48].

Functionals of the generalized-gradient-approximation (GGA) type combined with a dispersion correction are quite accurate for van der Waals complexes [55–60]. However, the majority of these dispersion corrections are less reliable for metal surfaces due to the empirical nature of the dispersion coefficients [61–66] and it has been argued that many-body effects may be important for accurate modeling of surface adsorption [67]. Non-local van der Waals density functionals (vdW-DF) [68–71] are typically more reliable for molecular physisorption on metal surfaces [66, 72]. Several groups [46, 47, 49] have studied adsorption of graphene on multiple metals using vdW-DF functionals; however, there are massive differences between the results depending on the base GGA functional used. For example, vdW-DF2 [71] (which uses revPBE [73]) predicts weak physisorption on Cu and Ni, while vdW-DF2-C09 [74] predicts stronger chemisorption [47]. The best available theoretical reference data for graphene adsorption is a study using the random phase approximation (RPA) by Olsen and Thygesen [48]. Though the RPA agrees with most experimental observations, the scope of this investigation was limited to a single Moiré pattern on each studied metal that minimized lattice strain [48], which precludes prediction of the orientation dependence [52].

This paper is the second part of a series [75] investigating graphene-metal adsorption using DFT paired with the exchange-hole dipole moment (XDM) dispersion correction [60, 76–79]. The XDM model is a non-empirical dispersion correction that uses the electron density to generate environment-dependent dispersion coefficients. As a result, XDM is uniquely suited to model dispersion interactions across a wide range of chemically diverse systems, such as molecular dimers [78, 80], supra-molecular systems [81], organic crystals [82, 83], and most closely related to this work, molecular physisorption [66]. The first part of this series was limited to graphene adsorp-

tion on nickel, for which XDM was found to provide excellent agreement with both RPA reference calculations and the experimental adsorption energy [75]. However, this is no guarantee that the high accuracy of XDM will be transferable to modeling graphene adsoprtion on other metals.

In the present work, we have broadened our study to include six additional metals: Al, Cu, Ag, Au, Pd, and Pt. The XDM results are found to more closely reproduce RPA interlayer distances and adsorption energies [48] than other, previously-applied density functionals. Additionally, this is the first dispersion-corrected DFT study to investigate graphene adsorption in two rotational orientations, corresponding to 0° and 30° Moiré patterns. It is shown that the graphene-substrate interaction strength is highly dependent on rotational orientation. The XDM calculations predict particularly strong graphene-surface interactions in the 0° orientation for Pd and Pt, which explain the experimental observation of multiple Moiré patterns with locally-ordered graphene domains. Finally, our results suggest that larger units cells (impractical for DFT calculations) are needed to properly model graphene-metal interactions for substrates with large surface-lattice mismatches.

2. Computational methods

The computational methods used here are consistent with our previous work on Ni(111)-graphene [75]. All DFT calculations were performed using periodic boundary conditions with the projector augmented wave (PAW) formalism [84] as implemented in Quantum ESPRESSO [78, 85]. The exchange-correlation functional chosen was B86bPBE [86, 87], as it provides the best accuracy when paired with the XDM dispersion model [66, 82]. An $8 \times 8 \times 1$ Γ-centered **k**-point grid was used, with a plane-wave cutoff of 60 Ry, a density expansion cutoff of 800 Ry, and cold smearing [88] with a smearing parameter of 0.01 Ry.

The XDM dispersion energy is a post-SCF correction to the B86bPBE (base) energy:

$$E = E_{\text{base}} + E_{\text{XDM}} \tag{1}$$

$$E_{\text{XDM}} = -\frac{1}{2} \sum_{n=6,8,10} \sum_{i \neq j} \frac{C_{n,ij} f_n(R_{ij})}{R_{ij}^n} \tag{2}$$

In this equation, i and j run over atoms in the system, R_{ij} is the interatomic distance, f_n is a damping function that attenuates the dispersion correction at short range, and the $C_{n,ij}$ are pairwise atomic

dispersion coefficients. Each $C_{n,ij}$ is evaluated using the multipole moments for the interacting atoms arising from a reference electron together with its corresponding exchange-hole distribution, as well as atom-in-molecule polarizabilities [60, 79].

In this work, calculations were performed for graphene adsorption on six metal surfaces: aluminum, copper, silver, gold, palladium, and platinum. Additionally, our previous results for nickel [75] are reported again here for comparative purposes. All calculations for the Ni-group metals used an initial spin-polarization, while those for Al and the Cu-group metals did not. All metals considered have a face-centered cubic (fcc) crystal structure and adsorption of graphene on the (111) surface was studied. Two different orientations, or Moiré patterns, were modeled to compare how rotational orientation affects graphene-substrate interactions. These were constructed using the (1×1) surface unit cell for the 0° orientation, where the lattice vectors of graphene's primitive cell align with the (111) metal surface's primitive cell (Figure 1b and c). The $(\sqrt{3} \times \sqrt{3})$ surface unit cell was obtained by rotating the metal substrate by 30° relative to the graphene sheet (Figure 1a). Both of these orientations have been established in previous works [45–48], with the (1×1) cell commonly used for Ni and Cu and the $(\sqrt{3} \times \sqrt{3})$ cell used for the remaining metals to minimize lattice strain.

Geometries for graphene adsorbed in the 30° orientation and two of the possible structures (top-fcc and fcc-hcp, using the common nomenclature [42, 46–48, 75]) for the 0° orientation are illustrated in Figure 1. Calculations were also performed for the four remaining structures in the 0° orientation (bridge-fcc, bridge-hcp, bridge-top, and top-hcp). The larger $(\sqrt{3} \times \sqrt{3})$ cell for the 30° orientation results in a periodic graphene layer with eight carbon atoms per cell, as the graphene unit cell is 2 times longer in each direction compared to the 0° orientation. The carbon atoms are equally split over void and on-top sites, such that the interactions are degenerate upon *x*-*y* translation, and only the structure shown in Figure 1(a) need be considered. In the following sections, the geometries for each of these cells will be discussed using the cell lengths represented in Figure 1. The relations between these quantities are: $a_{1\times1} = r$, $a_{\sqrt{3}\times\sqrt{3}} = r\sqrt{3}$, $a_{\text{cubic}} = r\sqrt{2}$, where r is the nearest-neighbor metal-metal distance, a_{cubic} is the cell length of the conventional (cubic) cell for the bulk metal (fcc), and $a_{1\times1}$ and $a_{\sqrt{3}\times\sqrt{3}}$ are the cell lengths of the (1×1) and $(\sqrt{3} \times \sqrt{3})$ cells, respectively, as depicted in Figure 1. The primitive cell length of graphene is

Figure 1: Structure of graphene adsorbed on a (111) metal surface for (a) the ($\sqrt{3} \times \sqrt{3}$) unit cell (30° rotation, see text) and (b,c) two selected translational orientations in the (1×1) unit cell (0° rotation). The metal top layer is shown in light gray, the second layer is blue, and the third layer from the surface is green. Unit cells for the 0° and 30° rotations are shown in red.

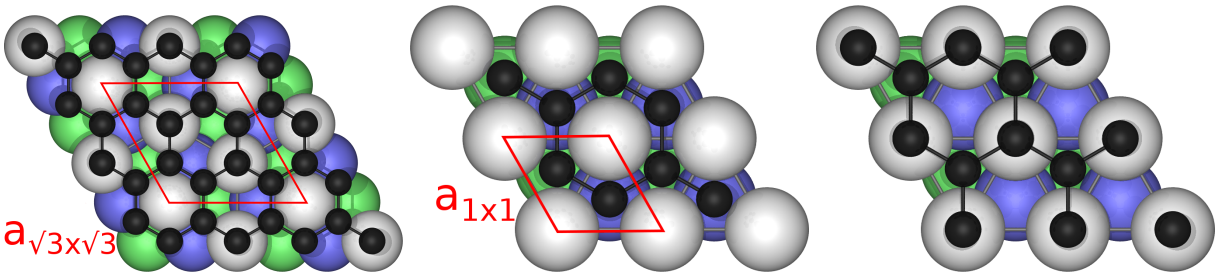

(a) ($\sqrt{3} \times \sqrt{3}$) (b) (1×1) fcc-hcp (c) (1×1) top-fcc

matched to the (1×1) cell on the metal surface, and a 2×2 graphene supercell matches the metal surface's ($\sqrt{3} \times \sqrt{3}$) cell.

Potential energy curves for graphene adsorption were computed for all metals. As in our previous work for nickel [75], the metal was represented by a six-layer slab and a cell 70 atomic units long in the vacuum direction to separate each slab from its periodic image. The adsorption energies are defined as:

$$E_{\text{ads}} = -\left[E_{\text{surf+graph}}(a^{\text{ads}}) - E_{\text{surf}}(a^{\text{surf}}) - E_{\text{graph}}(a^{\text{graph}})\right], \tag{3}$$

where $E_{\text{surf+graph}}(a^{\text{ads}})$ is the energy of the graphene plus metal system at its equilibrium geometry (a^{ads}) in the chosen orientation, and $E_{\text{surf}}(a^{\text{surf}})$ and $E_{\text{graph}}(a^{\text{graph}})$ are the energies of the metal surface and graphene at their respective minimum-energy geometries. Occasionally, two adsorption energies are possible when chemisorption and physisorption minima coexist on the same potential energy surface [75].

In addition, to allow direct comparison between the results for the (1×1) and ($\sqrt{3} \times \sqrt{3}$) cells, we define the constrained adsorption energy as:

$$E_{\text{ads}}^{\text{cons}} = -\left[E_{\text{surf+graph}}(a^{\text{ads}}) - E_{\text{surf}}(a^{\infty}) - E_{\text{graph}}(a^{\infty})\right], \tag{4}$$

where $E_{\text{surf}}(a^{\infty})$ and $E_{\text{graph}}(a^{\infty})$ are the energies of the infinitely separated metal surface and the graphene sheet, constrained to have the same lattice constant (a^{∞}). The sum of these two energies

is easily obtained as the surface lattice constant that minimizes the total value of $E_{\mathrm{surf}}(a)+E_{\mathrm{graph}}(a)$, where the surface and graphene energies are calculated independently. Relaxed, not constrained, adsorption energies were reported in our previous study of graphene adsorption on nickel [75]. The lattice strain energy is defined as the difference between the constrained and the relaxed adsorption energies:

$$E^{\mathrm{strain}} = [E_{\mathrm{surf}}(a^{\infty}) - E_{\mathrm{surf}}(a)] + \left[E_{\mathrm{graph}}(a^{\infty}) - E_{\mathrm{graph}}(a)\right], \tag{5}$$

The strain energy is always positive, and it is low compared to the constrained adsorption energy only when graphene and metal surface have matching lattices in the selected orientation. Positive adsorption energies indicate favorable adsorption relative to the separated surfaces.

Due to current limitations regarding the calculation of XDM forces for the particular case of metal surfaces [75], the minimum-energy structures were determined by calculating multiple adsorption potential energy surfaces, varying the surface lattice constants in 0.01 Å intervals. Minimum-energy PES were obtained by performing quadratic fits to the energy as a function of surface lattice constant at every graphene-metal distance. This procedure determines the minimum-energy surface lattice constant, graphene-metal distance, and adsorption energy. Throughout the article, adsorption energies are reported in kJ/mol per carbon atom.

Finally, the extent of charge transfer between metal and graphene was investigated using Bader's Quantum Theory of Atoms in Molecules (QTAIM) [89, 90]. QTAIM atomic charges were calculated using the Yu-Trinkle algorithm [91] (YT) implemented in the CRITIC2 program [92]. The QTAIM charges for the carbon atoms of the adsorbed graphene sheet determine the degree of charge transfer.

3. Results and Discussion

3.1. Lattice constants and adsorption energies

The computed lattice constants for graphene, the bulk metals, and adsorbed graphene are compared to the available experimental values in Table 1. B86bPBE-XDM performs quite well for the lattice constants of the bulk metals, with errors for the conventional (cubic) cell length of 0.06 Å or less. Similarly, the errors are 0.08 Å or less for the (1×1) surface lattice constants.

Table 1: Comparison of calculated and experimental bulk and (111) surface lattice constants for the considered metals and graphene. All metals have a face-centered cubic (fcc) structure. The calculated surface lattice constants are reported for both the (1×1) and $(\sqrt{3} \times \sqrt{3})$ unit cells. The metal surfaces that minimize the strain energy, as defined in Eq. 5, are indicated in bold. Lattice constants are also given for the combined graphene+metal system for both the minimum-energy adsorbed configuration (a^{ads}) and for the infinitely separated constrained system (a^{∞}, Eq. 4). For Ni and Pt, chemisorption and physisorption minima are present. All lengths are in Å and all energies are in kJ/mol per carbon atom.

	Bulk		Clean surface			Graphene + metal					
	$a^{\text{expt}}_{\text{cubic}}$ [93]	a_{cubic}	$a^{\text{expt}}_{1\times1}$	$a_{1\times1}$	$a_{\sqrt{3}\times\sqrt{3}}$	$a^{\text{ads}}_{1\times1}$	$a^{\infty}_{1\times1}$	$E^{\text{strain}}_{1\times1}$	$a^{\text{ads}}_{\sqrt{3}\times\sqrt{3}}$	$a^{\infty}_{\sqrt{3}\times\sqrt{3}}$	$E^{\text{strain}}_{\sqrt{3}\times\sqrt{3}}$
Al	4.050	4.001	2.86[94]	2.855	**4.946**	2.721	2.722	75.6	4.931	4.930	**0.1**
Cu	3.615	3.576	2.56[95]	**2.555**	4.425	2.520	2.520	**4.1**	–	4.671	$-^{\infty}$
Ag	4.086	4.081	2.89[96]	2.944	**5.100**	2.818	2.817	116.1	5.030	5.023	**4.8**
Au	4.078	4.136	2.88[26]	2.956	**5.120**	2.858	2.858	128.4	5.045	5.049	**4.9**
Ni	3.524	3.462	2.49[97]	**2.477**	4.291	2.481, 2.466	2.464	**0.0**	–	4.574	–
Pd	3.890	3.933	2.75[28]	2.806	**4.856**	2.751	2.726	66.9	4.865	4.868	**1.8**
Pt	3.923	3.968	2.78[98]	2.822	**4.887**	2.787, 2.760	2.760	78.1	4.878	4.881	**1.1**
Graphene (calc.)				2.474	4.948						
Graphene (expt)				2.46[99]	4.92						

For the (1×1) cell, the lattice constants for the graphene-metal system are typically below the optimum values for the clean metal surface to reduce the lattice strain from stretching the graphene C-C bonds. The lattice mismatch between graphene and the metal surface results in highly stretched C-C bonds for Al, Ag, Au, Pd, and Pt in this orientation, which results in extremely high strain energies for these metals. As a result, previous DFT studies have all used a rotated $(\sqrt{3} \times \sqrt{3})$ unit-cell, corresponding to the 30° Moiré pattern, for all metals except Cu and Ni [45–48]. For this cell, the strain within the graphene sheet is minimized, with the C-C bonds stretched no more than 0.04 Å relative to their equilibrium values. In the $(\sqrt{3} \times \sqrt{3})$ orientation, the lattice constants for the graphene-metal system are quite close to the optimum values for the clean metal surfaces and the strain energies are low (5 kJ/mol or less) compared to their (1×1) counterparts. However, consideration of only the $(\sqrt{3} \times \sqrt{3})$ precludes prediction of interaction energies for an adsorbed layer with direct carbon-metal contacts, as occur for several orientations of the (1×1) cell. Graphene adsorption on Cu or Ni was not studied with the rotated $(\sqrt{3} \times \sqrt{3})$ unit cell due to the lack of experimental evidence of its existence and the highly compressed C-C bonds that would result from this geometry.

Table 2 shows the calculated constrained and relaxed adsorption energies for all metals and orientations. The results for Ni are reproduced from our previous study and are included for comparison, while all other results are original to the present work. In agreement with the lattice constants and strain energies in Table 1, the (1×1) orientation is stable for Ni and Cu only, and the $(\sqrt{3} \times \sqrt{3})$ is favorable for the rest of the metals. Importantly, only nickel and platinum present adsorption energies higher than the exfoliation energy of graphite [49, 75, 78] (experimental value = 5.1 kJ/mol [100]). The group 11 metals all show relatively low stabilization relative to the graphite exfoliation energy (Cu, 2.9 kJ/mol; Ag, 2.1 kJ/mol; Au, 1.5 kJ/mol). However, for a real surface, the graphene can adopt rotational orientations with much longer periodicity, or the surface can undergo reconstruction, to further reduce the lattice strain. Unfortuately, such orientations cannot be modeled practically with DFT methods due to the very large unit-cell dimensions required. As is common practice in DFT studies, the remainder of this work will focus on the constrained adsorption energies, which should provide a more representative view of the local graphene-metal interactions.

Table 2 shows striking differences in the graphene-metal interaction strengths between metals in group 10 and 11. Whereas Ni and Cu have similar constrained adsorption energies (slightly larger for Ni), Pt and particularly Pd show a strong tendency towards chemisorption that is absent in their group-11 counterparts (Au and Ag, respectively). Despite this, the lack of a suitable orientation makes Pt and Pd unable to bind graphene strongly, due to the very high strain energy. These results serve to reconcile some of the experimental observations [29, 36] where Pt and Pd show either weak or strong adsorption, depending on the orientation (see Section 3.6). It should also be noted that both the graphene and the Pd and Pt surfaces are severely distorted in the 1×1 orientation, which may increase their reactivity (although the same effect is not observed on Ag and Au).

3.2. Potential energy surfaces

Computed B86bPBE-XDM PES for adsorption of graphene on all seven metals are shown in Figure 2 for all six orientations of the (1×1) cell and for the $(\sqrt{3} \times \sqrt{3})$ cell. To compare the behavior of all orientations in the same plot, constrained adsorption energies are used. The dotted lines correspond to orientations with significant lattice strain (which would otherwise appear at much higher energies). As shown in the Supplementary Material, the dispersion contribution to the PES is effectively independent of the orientation. Hence, the differences in the PES between the various orientations are primarily due to differences in the direct C-metal contacts and the extent of *d*-band hybridization and charge transfer (Section 3.4) arising at the base-functional level.

For the (1×1) cell, the PES in Figure 2 show local chemisorption minima for all three Ni-group metals in the top-fcc, top-hcp and bridge-top orientations. For Pd, there is also chemisorption in the bridge-fcc and bridge-hcp orientations, although it is significantly weaker. As noted in our previous study on the Ni surface [75], chemisorption is made possible by the direct C-metal atomic contacts, as are present for top-fcc, top-hcp and bridge-top. However, only physisorption is seen for the fcc-hcp orientation, in which graphene C atoms are all above surface voids. Chemisorption similarly does not occur for the $(\sqrt{3} \times \sqrt{3})$ unit cell, for which the adsorption PES are nearly equivalent to the fcc-hcp curves for Pd and Pt. Therefore, it is the graphene-carbon interaction, or lack thereof, that results in the presence of a chemisorption minima for the Ni-group metals,

likely arising from the hybridization between the graphene p orbitals and the d band of the metal surface. Although the chemisorption minima are relatively much deeper for Pd and Pt than for Ni, the lattice mismatches prevent clean monolayer formation on these metals.

For Al and the Cu-group metals, the PES in Figure 2 show no chemisorption minima. Compared to the Ni-group metals, the d bands of the Cu-group are lower in energy relative to the Fermi level, which precludes hybridization with graphene's p orbitals. Therefore, the differences between the six possible (1×1) orientations are much smaller than for the Ni-group, with the net adsorption energies varying by 0.5-0.6 kJ/mol C between the various orientation for Al and Cu. These differences increase somewhat for the other two members of the group, with a spread between the most- and least-stable orientations of 1.0 kJ/mol C for Au and 1.5 kJ/mol C for Ag. It is more energetically favorable for the carbon atoms to lie directly above the surface atoms rather than the void sites, resulting in deeper PES for the top-fcc, top-hcp and bridge-top orientations than for the fcc-hcp orientation, in which there are no direct C-metal contacts (Figure 1). The $(\sqrt{3} \times \sqrt{3})$ PES are significantly more shallow than the (1×1) PES for Al and Ag. As will be shown in Section 3.4, this is due to the significant surface-substrate charge transfer that occurs in the (1×1) cell for Al and Ag at the physisorption minima. Al and Ag have the lowest work functions of the series of metals considered.

Table 2: Constrained ($E_{\text{ads}}^{\text{cons}}$, Eq. 4) and relaxed ($E_{\text{ads}}$, Eq. 3) adsorption energies for all metals and orientations in this work. The "Type" column indicates whether the entry is a physisorption (P) or chemisorption (C) minimum. Negative energies reflect that the orientation is not energetically stable. The maximum constrained and relaxed adsorption energies for each metal are indicated in bold. The units are kJ/mol per carbon atom.

		Al		Cu		Ag		Au	
Orientation	Type	$E_{\text{ads}}^{\text{cons}}$	E_{ads}	$E_{\text{ads}}^{\text{cons}}$	E_{ads}	$E_{\text{ads}}^{\text{cons}}$	E_{ads}	$E_{\text{ads}}^{\text{cons}}$	E_{ads}
1×1 bridge-fcc	P	4.2	-71.4	6.8	2.6	9.1	-107.0	7.2	-121.2
1×1 bridge-hcp	P	4.3	-71.3	6.7	2.6	9.1	-107.1	7.2	-121.3
1×1 bridge-top	P	4.4	-71.3	7.0	2.8	9.6	-106.5	7.5	-120.9
1×1 fcc-hcp	P	4.1	-71.6	6.5	2.3	8.4	-107.8	6.7	-121.7
1×1 top-fcc	P	4.2	-71.4	**7.1**	**2.9**	**9.9**	-106.3	**7.7**	-120.7
1×1 top-hcp	P	**4.6**	-71.0	7.0	2.9	9.7	-106.4	7.6	-120.8
$\sqrt{3} \times \sqrt{3}$	P	3.2	**3.2**	—	—	6.9	**2.1**	6.4	**1.5**
Orientation	Type	Ni		Pd		Pt			
		$E_{\text{ads}}^{\text{cons}}$	E_{ads}	$E_{\text{ads}}^{\text{cons}}$	E_{ads}	$E_{\text{ads}}^{\text{cons}}$	E_{ads}		
1×1 bridge-fcc	C	—	—	10.2	-56.7	—	—		
	P	8.0	8.0	—	—	6.9	-71.3		
1×1 bridge-hcp	C	—	—	9.8	-57.1	—	—		
	P	8.0	8.0	—	—	6.8	-71.4		
1×1 bridge-top	C	7.3	7.3	**20.5**	-46.5	**14.6**	-63.5		
	P	8.3	8.3	—	—	7.3	-70.9		
1×1 fcc-hcp	P	7.5	7.5	6.7	-60.2	6.4	-71.8		
1×1 top-fcc	C	**7.8**	**7.8**	16.3	-50.7	7.8	-70.3		
	P	**8.5**	**8.5**	—	—	**7.6**	-70.6		
1×1 top-hcp	C	6.5	6.5	14.9	-52.0	5.9	-72.3		
	P	8.4	8.4	—	—	7.2	-71.0		
$\sqrt{3} \times \sqrt{3}$	P	—	—	6.3	**4.5**	6.8	**5.7**		

Figure 2: Computed B86bPBE-XDM PES for adsorption of graphene on selected metals in the ($\sqrt{3} \times \sqrt{3}$) cell and all six possible orientations of the (1 × 1) cell. The left column shows results for the Ni-group metals, while the right column shows results for Al and the Cu-group metals. Constrained adsorption energies are used in this plot (i.e. metal and graphene are forced to have the same surface lattice constant at infinite separation). The orientations with significant lattice mismatch, which would be much higher in energy if the relaxed adsorption energies were used, are shown as dotted curves.

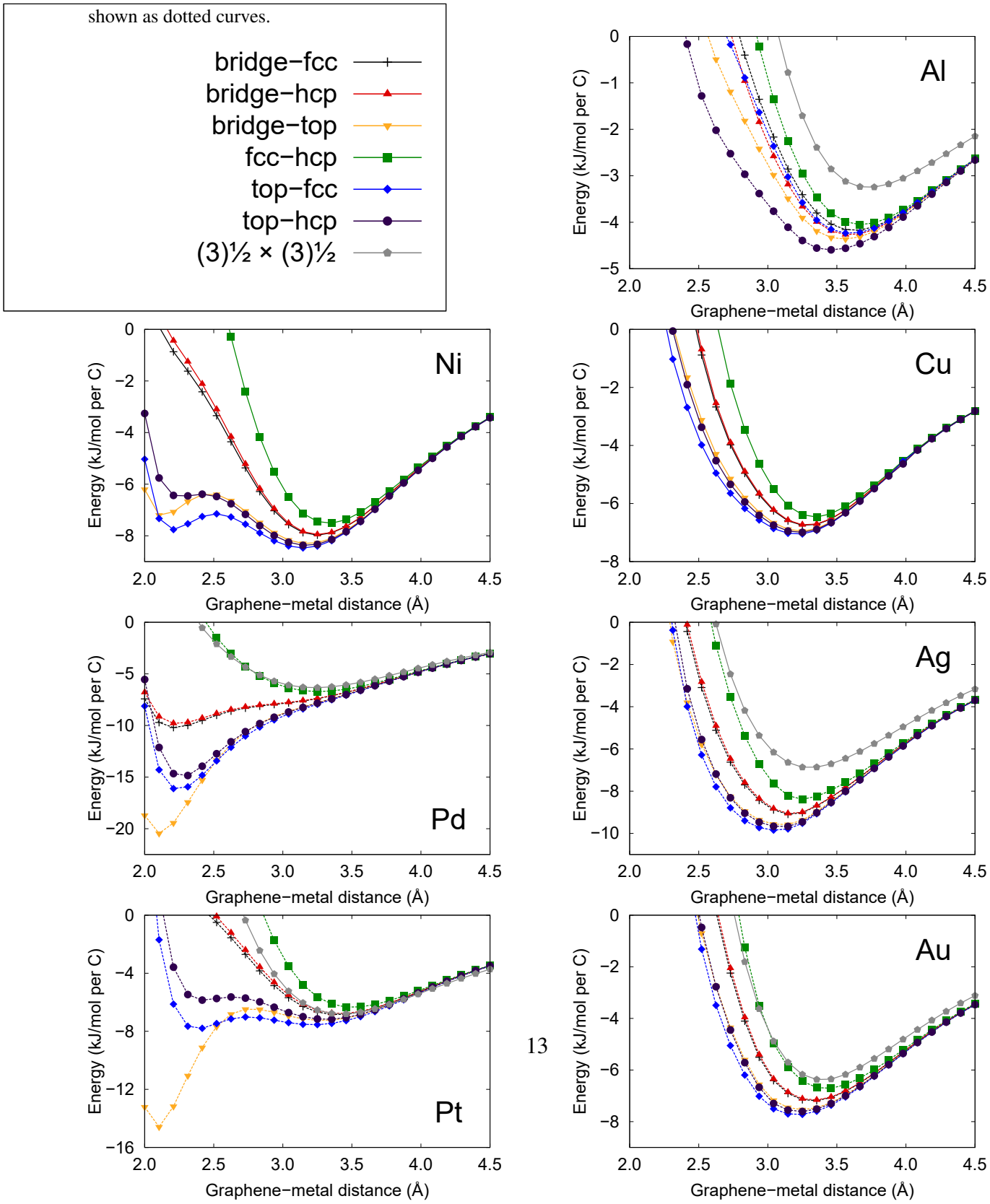

3.3. Dispersion and periodic trends

Optimal B86bPBE-XDM graphene-metal interlayer distances and metal-carbon C_6 dispersion coefficients are reported in Table 3. The C_6 dispersion coefficients are the main factor that determines the equilibrium distances and adsorption energies at the physisorption minima. The optimum interlayer distances for the physisorption minima are nearly degenerate for each periodic row, due to the similar atomic sizes. Al has the lowest C_6 coefficient, resulting in the lowest physisorption energy and the largest interlayer distance. The C_6's, optimum interlayer distances, and binding energies generally increase down the periodic groups, with the exception of Au and Pt, for which the C-metal C_6 and graphene adsorption energy are lower than for Ag and Pd, respectively. This is due to relativistic effects, which cause Au/Pt to be significantly more electronegative than Ag/Pd, resulting in a lower polarizability and weaker dispersion attraction [66, 101].

Ni and Pt display both chemisorption and physisorption minima, while graphene only chemisorbs on Pd. This occurs because of a combination of a higher base-functional contribution to the adsoprtion PES due to *d*-band hybridization and charge transfer (see Section 3.4) and a lower dispersion contribution to the adsorption energy due to a smaller C-metal C_6 coefficient for Pd (Table 3). For metals with both chemisorbed and physisorbed minima, the C_6's are typically smaller for the former, because of the partial positive charge on the surface atoms that result from metal-graphene charge transfer. Lastly, the carbon-metal dispersion coefficients are slightly larger for physisorbed minima in the (1×1) cell than for the $(\sqrt{3} \times \sqrt{3})$ cell due to the larger lattice constants in the former, which result in stretched C-C bonds.

3.4. Charge transfer

QTAIM results for the extent of metal-to-graphene charge transfer are presented in Table 4. Generally the extent of charge transfer is inversely related to the graphene-surface distance, with the 1×1 bridge-top orientation giving the largest charge transfer, followed by 1×1 top-fcc. In our previous work on Ni, only the chemisorbed orientations showed significant charge transfer [75] and the present results indicate negligible charge transfer for all physisorption minima in the $(\sqrt{3} \times \sqrt{3})$ cell. However, considerable charge transfer is seen for several physisorption minima in the (1×1) unit cell of metals other than Ni, particularly for Al and Ag (which have the lowest

Table 3: Calculated B86bPBE-XDM carbon-metal C_6 dispersion coefficients (in a.u.), minimum-energy interlayer distances (in Å), and constrained adsorption energies (in kJ/mol C) for both (1×1) and $(\sqrt{3} \times \sqrt{3})$ surface unit cells of selected metals. Chemisorption states are denoted with a C and physisorption states are denoted with a P.

Metal	Orientation	Type	C_6 (a.u)	d (Å)	E_{ads}^{cons} (kJ/mol C)
Al	1×1 top-hcp	P	34.7	3.48	4.6
	$\sqrt{3} \times \sqrt{3}$	P	36.4	3.75	3.2
Cu	1×1 top-fcc	P	42.8	3.22	7.1
Ag	1×1 top-fcc	P	61.2	3.06	9.9
	$\sqrt{3} \times \sqrt{3}$	P	59.4	3.31	6.9
Au	1×1 top-fcc	P	60.3	3.22	7.7
	$\sqrt{3} \times \sqrt{3}$	P	56.5	3.41	6.4
Ni	1×1 top-fcc	C	39.3	2.22	7.8
	1×1 top-fcc	P	44.1	3.15	8.5
Pd	1×1 bridge-top	C	38.6	2.12	20.5
	$\sqrt{3} \times \sqrt{3}$	P	43.1	3.24	6.3
Pt	1×1 bridge-top	C	45.9	2.10	14.6
	1×1 top-fcc	P	54.3	3.22	7.6
	$\sqrt{3} \times \sqrt{3}$	P	51.5	3.44	6.8

work functions), indicating that the stretched C-C bonds make charge transfer more favorable. This result explains why the PES in Figure 2 show significantly less binding for Al and Ag in the $(\sqrt{3} \times \sqrt{3})$ configuration as compared to (1×1) fcc-hcp.

Pd has the largest charge transfer of all metals; taken together with its relatively low dispersion coefficient (Table 3) and its readiness to form covalent bonds to graphene's p orbitals, this explains the presence of only a single deep chemisorption minimum for most (1×1) orientations. Generally, charge transfer from the metal is proportional to the interlayer distances and adsorption energies, with Pd>Pt>Ni. LEED studies have previously shown evidence of strong interactions between graphene and these metals in commensurate orientations [29, 31, 36]. Additionally, a tribology

Table 4: Charge transfer from the metal to the graphene layer (per C) obtained from QTAIM analysis of the B86bPBE electron densities.

Metal	Type	bridge-fcc	bridge-hcp	bridge-top	fcc-hcp	top-fcc	top-hcp	$\sqrt{3}\times\sqrt{3}$
Al	P	0.019	0.020	0.022	0.018	0.020	0.024	0.008
Cu	P	0.003	0.003	0.004	0.003	0.005	0.004	–
Ag	P	0.021	0.021	0.022	0.023	0.023	0.021	0.008
Au	P	0.008	0.008	0.009	0.007	0.010	0.010	0.000
Ni	C	–	–	0.054	–	0.047	0.042	–
	P	0.003	0.003	0.003	0.003	0.004	0.003	–
Pd	C	0.044	0.043	0.051	–	0.043	0.040	–
	P	–	–	–	0.004	–	–	0.000
Pt	C	–	–	0.049	–	0.028	0.024	–
	P	0.000	0.000	0.000	0.001	0.001	0.000	-0.006

experiment [36] involving graphene on platinum has shown graphene interacts more strongly with the metal substrate under stress, suggesting that greater charge-transfer is achievable with even closer graphene-metal contacts.

3.5. Comparison with previous theory

Previous density-functional studies of graphene adsorption limited their scope to the (1×1) cell for Cu and Ni and the ($\sqrt{3}\times\sqrt{3}$) cell for other metals in order to minimize C-C bond distortion. Our B86bPBE-XDM results for the minimum-energy graphene-metal separations and constrained adsorption energies are compared with selected results from previous theoretical studies in Table 5. Literature data is reported for the RPA [48], two vdw-DF functionals [47] and the LDA [46, 48].

Table 5 shows that B86bPBE-XDM is in the closest agreement with RPA [48] for both interlayer distances and binding energies. This adds to our previous results showing excellent agreement between B86bPBE-XDM and the RPA for graphene adsorption on Ni [75] and for graphite exfoliation [75, 78].

Table 5: Constrained adsorption energies ($E_{\text{ads}}^{\text{cons}}$ in kJ/mol C) and interlayer distances (d in Å) for graphene on selected metal surfaces. Data for Cu and Ni is given for the top-fcc orientation of the (1×1) cell while all other metals use the $(\sqrt{3} \times \sqrt{3})$ cell. The B86bPBE-XDM results are from the present work, except for Ni, where the values are correspond to the chemisorbed minimum from Ref. 75; all other results are from the literature. Two sets of LDA results are given, using either relaxed [46] or experimental lattice parameters [48].

		LDA [46, 48]	vdw-DF2 [47]	vdw-DF2-C09 [47]	RPA [48]	B86bPBE-XDM
Al	d	3.44, 3.46	–	–	3.51	3.75
	E_{ads}	2.41, 2.80	–	–	5.02	3.25
Cu	d	2.21, 3.21	3.73	2.94	3.09	3.22
	E_{ads}	3.38, 6.95	4.44	5.98	6.56	7.05
Ag	d	3.22, 3.32	3.73	3.23	3.31	3.31
	E_{ads}	2.89, 4.34	4.05	5.11	7.53	6.90
Au	d	3.32, 3.35	3.69	3.29	3.22	3.41
	E_{ads}	2.99, 3.28	4.73	5.69	9.17	6.40
Ni	d	2.00, 2.08	3.68	2.07	2.19	2.22
	E_{ads}	11.87, 18.14	4.25	13.60	6.75	7.79
Pd	d	2.33, 3.00	3.59	2.92	3.34	3.24
	E_{ads}	4.15, 7.62	5.02	6.95	8.68	6.34
Pt	d	3.25, 3.35	3.71	3.24	3.42	3.44
	E_{ads}	3.18, 3.47	5.21	6.56	8.10	6.81

The LDA tends to under-estimate the adsorption energies relative to both B86bPBE-XDM and the RPA for physisorption, as expected due to the neglect of dispersion. Additionally, the LDA predicts chemisorption minima for Cu and Pd, which are not present with either B86bPBE-XDM or the RPA, and the chemisorption energy on Ni is significantly over-estimated. The two sets of LDA results differ significantly depending on whether relaxed lattice parameters [46] or experimental lattice parameters [48] were used in the calculations.

While several authors [46–48] have performed calculations on these systems with the original vdw-DF1 method [102], we focus on the more-recent vdw-DF2 [71] and vdw-DF2-C09 [74], which are typically more accurate [103]. The vdw-DF2 results appear to systematically underbind, predicting longer interlayer distances and lower adsorption energies than B86bPBE-XDM or the RPA. Conversely, vdw-DF2-C09 significantly under-estimates the interlayer distances and, like the LDA, drastically overestimates the energy for graphene chemisorption on Ni.

3.6. Connection with experiment

Our calculations along with previous experimental results [28–34, 36], and one LDA study [52], suggest that the interaction between graphene and both Pd and Pt is strongly dependent on the graphene-metal orientation. Our calculated adsorption energies in Table 2 explain conflicting experimental observations that graphene forms both strong [28] and weak [30] interactions with the Pd surface. Notably, Murata *et al.* [29] observed a strong dependence on rotational orientation; the 30° orientation interacts weakly with the surface and the interaction strength is proportional to the alignment between the substrate and surface lattice constants. Similarly, it has been found that the lattice mismatch results in formation of graphene ripples on Pt surfaces, leading to strong local interactions [27, 31, 33, 36], but weak interactions overall [32, 34]. While our results predict strong chemisorption of graphene in the bridge-top orientation of the (1×1) cell, the energy penalty due to C-C bond strain is prohibitive for graphene to adopt this orientation globally, in agreement with experiment [33]. However, our results suggest that strong chemisorption behavior is possible locally between individual carbon and Pd/Pt atoms, or between small domains with favorable atomic alignment. For physisorbed orientations of graphene on Pt, the global average interlayer distance was found to be 3.30 Å [32], which is intermediate between the distances of 3.21 Å and 3.44 Å for the (1×1) and $(\sqrt{3} \times \sqrt{3})$ cells predicted by B86bPBE-XDM (Table 3).

In contrast to the Ni-group, the constrained results in Table 2 show that graphene physisorbs on each of the coinage metals regardless of the rotational orientation on the surface. This is consistent with LEED and STM experiments that have shown that graphene interacts with copper and gold weakly [37, 38, 95, 104, 105]. Also, the (1×1) constrained adsorption energies are generally greater than for the $(\sqrt{3} \times \sqrt{3})$ cell (Table 2). This is in agreement with experiments showing that

graphene prefers the strained 0° orientation instead of the less-strained 30°-rotated Moiré pattern on Au. To minimize the C-C bond strain, the graphene sheet is observed to fold into a herringbone orientation [37, 38].

Our results suggest that there is a significant energetic drive for graphene to adopt an aligned on-top orientation on a substrate's surface. This interaction drives the initial Moiré structure formation until the graphene sheet grows large enough so that either the surface or graphene reconstruct globally to minimize the C-C bond strain, as occurs on Pd, Pt, and Au.

4. Summary

This paper studied graphene adsorption on seven different (111) face-centered cubic metal surfaces (Al, Ni, Pd, Pt, Cu, Ag, and Au). The 0° orientation, corresponding to a (1×1) surface unit cell was studied for all seven metals, using six different graphene-metal geometries (top-fcc, top-hcp, fcc-hcp, bridge-top, bridge-hcp, and bridge-fcc, in the usual nomenclature [42, 46–48, 75]). In addition, the 30° orientation, corresponding to a $(\sqrt{3} \times \sqrt{3})$ surface unit cell, was also studied for all metals except Ni and Cu. The exchange-hole dipole moment (XDM) dispersion correction combined with the B86bPBE functional was used, and our calculations were compared to previous theoretical and experimental observations. In particular, excellent agreement is found between B86bPBE-XDM and reported RPA adsorption energies and graphene-metal distances.

Our results show that graphene-substrate interactions depend both on rotational orientation and lattice commensurability. Ni and Cu have lattices that match graphene in the (1×1) surface unit cell, whereas the remaining metals match with graphene in the $(\sqrt{3} \times \sqrt{3})$ cell. Surface adsorption is strongly unfavorable in the incommensurate orientations due to the high lattice strain. Experimentally, graphene can adopt rotational orientations with longer periodicity to reduce this lattice strain. However, to obtain proper energy rankings of Moiré patters on these substrates, much larger unit cells than can be efficiently modeled with DFT are required.

To quantify physisorption and chemisorption effects as a function of graphene-metal distance, the lattice strain energy was eliminated from the adsorption energy by taking the graphene and metal contributions to correspond to an infinitely separated graphene sheet and metal surface, constrained to have equal lattice constants. This "constrained" adsorption energy is largest in the

(1×1) unit cell, which maximizes direct on-top contacts between the graphene carbon atoms and underlying surface metal atoms. The results for the (1×1) cell showed that Pt displays both physisorption and chemisorption minima for the top-fcc, top-hcp, and bridge-top orientations. This behavior is similar to Ni, although the chemisorption interaction is stronger on Pt. Only chemisorption minima occur for Pd in the on-top orientations due to greater charge transfer and weaker dispersion interactions relative to Pt. Conversely, only physisorption is observed for the noble metals and Al, where there are only small energy differences on the order of $\sim$ 1 kJ/mol C between the various (1×1) orientations. In the rotated ($\sqrt{3} \times \sqrt{3}$) cell, only physisorption minima are present for all metals considered. Because half of the graphene carbon atoms reside over voids, the ($\sqrt{3} \times \sqrt{3}$) adsorption PES resemble those for the fcc-hcp orientation of the (1×1) cell. The dispersion coefficients and adsorption-energy contributions are nearly invariant with respect to both graphene rotation and lateral translation, indicating that the changes in PES arise due to the presence or absence of direct C-metal contacts.

Our results indicate that there is a strong driving force for graphene to align with the surface, particularly for the Ni-group metals. This explains the observation that the 0° Moiré pattern is dominant on gold despite the high degree of C-C bond strain. Experimentally, it appears that the graphene's lattice strain is reduced by adoption of a herringbone orientation on the surface [37, 38]. The energetic drive for local surface-substrate alignment, along with incommensurate graphene-metal lattice constants is the likely cause for formation of multiple Moiré patterns on metal surfaces. In particular, the combination of the strong chemisorption seen on Pd and Pt in the incommensurate (1×1) cell and weak physisorption in the commensurate ($\sqrt{3} \times \sqrt{3}$) cell explains experimental observations that graphene has multiple Moiré patterns on Pd and Pt, forming strong interactions locally, but weak interactions globally [29, 30, 33–35].

Acknowledgement: We gratefully acknowledge the Natural Sciences and Engineering Research Council of Canada (NSERC) for financial support and Compute Canada (ACEnet and Westgrid) for computational resources.

5. References

[1] K. S. Novoselov, A. K. Geim, S. Morozov, D. Jiang, Y. Zhang, S. Dubonos, I. Grigorieva, A. A. Firsov, Electric field effect in atomically thin carbon films, Science 306 (2004) 666.

[2] A. H. Castro-Neto, F. Guinea, N. M. R. Peres, K. S. Novoselov, A. K. Geim, The electronic properties of graphene, Rev. Mod. Phys. 81 (2009) 109.

[3] A. K. Geim, K. S. Novoselov, The rise of graphene, Nat. Mater. 6 (2007) 183.

[4] P. Plachinda, D. R. Evans, R. Solanki, Electronic properties of metal-arene functionalized graphene, J. Chem. Phys. 135 (2011) 044103.

[5] S. Das Sarma, S. Adam, E. H. Hwang, E. Rossi, Electronic transport in two-dimensional graphene, Rev. Mod. Phys. 83 (2011) 407.

[6] V. Singh, D. Joung, L. Zhai, S. Das, S. I. Khondaker, S. Seal, Graphene based materials: Past, present and future, Prog. Mater. Sci. 56 (2011) 1178.

[7] S. Guo, S. Dong, Graphene nanosheet: synthesis, molecular engineering, thin film, hybrids, and energy and analytical applications, Chem. Soc. Rev. 40 (2011) 2644.

[8] Z. Xu, Q. Zhang, X. Shi, W. Zhai, Q. Zhu, Comparison of Tribological Properties of NiAl Matrix Composites Containing Graphite, Carbon Nanotubes, or Graphene, J. Mater. Eng. Perform. 24 (2015) 1926.

[9] M. S. Won, O. V. Penkov, D. E. Kim, Durability and degradation mechanism of graphene coatings deposited on Cu substrates under dry contact sliding, Carbon 54 (2013) 472.

[10] H. Chen, T. Filleter, Effect of structure on the tribology of ultrathin graphene and graphene oxide films, Nanotech. 26 (2015) 135702.

[11] D. Berman, S. A. Deshmukh, S. K. Sankaranarayanan, A. Erdemir, A. V. Sumant, Extraordinary Macroscale Wear Resistance of One Atom Thick Graphene Layer, Adv. Funct. Mater. 24 (2014) 6640–6646.

[12] S. Cahangirov, S. Ciraci, V. O. Özçelik, Superlubricity through graphene multilayers between Ni(111) surfaces, Phys. Rev. B 87 (2013) 1.

[13] M. Tripathi, F. Awaja, G. Paolicelli, R. Bartali, E. Iacob, S. Valeri, S. Ryu, S. Signetti, G. Speranza, N. M. Pugno, Tribological characteristics of few-layer graphene over ni grain and interface boundaries, Nanoscale 8 (2016) 6646–6658.

[14] O. Penkov, H. J. Kim, H. J. Kim, D. E. Kim, Tribology of graphene: A review, Int. J. Precis. Eng. Manuf. 15 (2014) 577.

[15] K. S. Kim, H. J. Lee, C. Lee, S. K. Lee, H. Jang, J. H. Ahn, J. H. Kim, H. J. Lee, Chemical vapor deposition-grown graphene: The thinnest solid lubricant, ACS Nano 5 (2011) 5107–5114.

[16] A. Dianat, D. A. Ryndyk, G. Cuniberti, Contact-dependent mechanical properties of graphene nanoribbons: an ab-initio study, Nanotech. 27 (2016) 025702.

[17] J. C. Spear, B. W. Ewers, J. D. Batteas, 2D-nanomaterials for controlling friction and wear at interfaces, Nano

Today 10 (2015) 301–314.

[18] M. Batzill, The surface science of graphene: Metal interfaces, CVD synthesis, nanoribbons, chemical modifications, and defects, Surf. Sci. Rep. 67 (2012) 83.

[19] L. Zhao, K. T. Rim, H. Zhou, R. He, T. F. Heinz, A. Pinczuk, G. W. Flynn, A. N. Pasupathy, Influence of copper crystal surface on the CVD growth of large area monolayer graphene, Solid State Commun. 151 (2011) 509.

[20] R. Muñoz, C. Gómez-Aleixandre, Review of CVD synthesis of graphene, Chem. Vap. Depos. 19 (2013) 297.

[21] J. Coraux, A. T. N'Diaye, M. Engler, C. Busse, D. Wall, N. Buckanie, F. J. Meyer Zu Heringdorf, R. Van Gastel, B. Poelsema, T. Michely, Growth of graphene on Ir(111), New J. Phys. 11 (2009) 565.

[22] N. Bartelt, K. McCarty, Graphene growth on metal surfaces, MRS Bull. 37 (2012) 1158.

[23] L. Kong, A. Enders, T. S. Rahman, P. a. Dowben, Molecular adsorption on graphene, J. Phys. Condens. Matter 26 (2014) 443001.

[24] J. Wintterlin, M. L. Bocquet, Graphene on metal surfaces, Surf. Sci. 603 (2009) 1841–1852.

[25] C. Mattevi et al., A review of chemical vapour deposition of graphene on copper, J. Mater. Chem. 21 (2011) 3324–3334.

[26] T. Oznuluer, E. Pince, E. O. Polat, O. Balci, O. Salihoglu, C. Kocabas, Synthesis of graphene on gold, Appl. Phys. Lett. 98 (2011) 183101.

[27] H. Ueta, M. Saida, C. Nakai, Y. Yamada, M. Sasaki, S. Yamamoto, Highly oriented monolayer graphite formation on Pt(1 1 1) by a supersonic methane beam, Surf. Sci. 560 (2004) 183–190.

[28] S. Y. Kwon, C. V. Ciobanu, V. Petrova, V. B. Shenoy, J. Bareño, V. Gambin, I. Petrov, S. Kodambaka, Growth of semiconducting graphene on palladium, Nano Lett. 9 (2009) 3985–3990.

[29] Y. Murata, E. Starodub, B. B. Kappes, C. V. Ciobanu, N. C. Bartelt, K. F. McCarty, S. Kodambaka, Orientation-dependent work function of graphene on Pd(111), Appl. Phys. Lett. 97 (2010) 2014–2017.

[30] J. H. Gao, N. Ishida, I. Scott, D. Fujita, Controllable growth of single-layer graphene on a Pd(1 1 1) substrate, Carbon 50 (2012) 1674–1680.

[31] M. Sasaki, Y. Yamada, Y. Ogiwara, S. Yagyu, S. Yamamoto, Moiré contrast in the local tunneling barrier height images of monolayer graphite on Pt(111), Phys. Rev. B 61 (2000) 15653–15656.

[32] P. Sutter, J. T. Sadowski, E. Sutter, Graphene on Pt(111): Growth and substrate interaction, Phys. Rev. B 80 (2009) 1–10.

[33] P. Merino, M. Svec, A. L. Pinardi, G. Otero, Strain-Driven Moire Superstructures of Epitaxial Graphene on Transition, ACS Nano 5 (2011) 5627–5634.

[34] M. Gao, Y. Pan, L. Huang, H. Hu, L. Z. Zhang, H. M. Guo, S. X. Du, H. J. Gao, Epitaxial growth and structural property of graphene on Pt(111), Appl. Phys. Lett. 98 (2011) 3–6.

[35] I. Hernández-Rodríguez, J. M. García, J. A. Martín-Gago, P. L. de Andrés, J. Méndez, Graphene growth on Pt(111) and Au(111) using a MBE carbon solid-source, Diam. Relat. Mater. 57 (2015) 58–62.

[36] N. Chan, S. G. Balakrishna, A. Klemenz, M. Moseler, P. Egberts, R. Bennewitz, Contrast in nanoscale friction between rotational domains of graphene on Pt(111), Carbon 113 (2017) 132–138.

[37] A. J. Martínez-Galera, I. Brihuega, J. M. Gómez-Rodríguez, Ethylene irradiation: A new route to grow graphene on low reactivity metals, Nano Lett. 11 (2011) 3576–3580.

[38] J. M. Wofford, E. Starodub, A. L. Walter, S. Nie, A. Bostwick, N. C. Bartelt, K. Thürmer, E. Rotenberg, K. F. McCarty, O. D. Dubon, Extraordinary epitaxial alignment of graphene islands on Au(111), New J. Phys. 14 (2012) 053008.

[39] Y. Gamo, A. Nagashima, M. Wakabayashi, M. Terai, C. Oshima, Atomic Structure of Monolayer Graphite Formed on Ni(111), Hyomen Kagaku 17 (1996) 745.

[40] Y. Zhang, T. Gao, S. Xie, B. Dai, L. Fu, Y. Gao, Y. Chen, M. Liu, Z. Liu, Different growth behaviors of ambient pressure chemical vapor deposition graphene on Ni(111) and Ni films: A scanning tunneling microscopy study, Nano Res. 5 (2012) 402.

[41] W. Zhao, S. M. Kozlov, H. Oliver, K. Gotterbarm, M. P. A. Lorenz, F. Viñes, C. Papp, G. Andreas, H. P. Steinrück, Graphene on Ni (111): Coexistence of Different Surface Structures, J. Chem. Phys. Lett. 2 (2011) 759.

[42] F. Mittendorfer, A. Garhofer, J. Redinger, J. Klimeš, J. Harl, G. Kresse, Graphene on Ni(111): Strong interaction and weak adsorption, Phys. Rev. B 84 (2011) 2.

[43] A. Dahal, M. Batzill, Graphenenickel interfaces: a review, Nanoscale 6 (2014) 2548.

[44] X. Li, L. Colombo, R. S. Ruoff, Synthesis of Graphene Films on Copper Foils by Chemical Vapor Deposition, Adv. Mater. 28 (2016) 6247–6252.

[45] G. Giovannetti, P. A. Khomyakov, G. Brocks, V. M. Karpan, J. van den Brink, P. J. Kelly, Doping graphene with metal contacts, Phys. Rev. Lett. 101 (2008) 026803.

[46] M. Vanin, J. Mortensen, A. Kelkkanen, J. Garcia-Lastra, K. Thygesen, K. Jacobsen, Graphene on metals: A van der Waals density functional study, Phys. Rev. B 81 (2010) 081408.

[47] I. Hamada, M. Otani, Comparative van der Waals density-functional study of graphene on metal surfaces, Phys. Rev. B 82 (2010) 153412.

[48] T. Olsen, K. S. Thygesen, Random phase approximation applied to solids, molecules, and graphene-metal interfaces: From van der Waals to covalent bonding, Phys. Rev. B 87 (2013) 1–13.

[49] P. Janthon, F. Viñes, S. M. Kozlov, J. Limtrakul, F. Illas, Theoretical assessment of graphene-metal contacts, J. Chem. Phys. 138 (2013) 244701.

[50] P. A. Khomyakov, G. Giovannetti, P. C. Rusu, G. Brocks, J. Van Den Brink, P. J. Kelly, First-principles study of the interaction and charge transfer between graphene and metals, Phys. Rev. B 79 (2009) 1.

[51] S. M. Kozlov, F. Viñes, A. Görling, Bonding mechanisms of graphene on metal surfaces, J. Phys. Chem. C 116 (2012) 7360–7366.

[52] B. B. Kappes, A. Ebnonnasir, S. Kodambaka, C. V. Ciobanu, Orientation-dependent binding energy of graphene on palladium, Appl. Phys. Lett. 102 (2013) 5–10.

[53] A. F. Kuloglu, B. Sarikavak-Lisesivdin, S. B. Lisesivdin, E. Ozbay, First-principles calculations of Pd-terminated symmetrical armchair graphene nanoribbons, Comput. Mater. Sci. 68 (2013) 18–22.

[54] T. Chanier, L. Henrard, From carbon atom to graphene on Cu(111): an ab-initio study, Eur. Phys. J. B 88 (2015) 31.

[55] G. A. DiLabio, A. Otero-de-la Roza, Dispersion interactions in density-functional theory, Rev. Comp. Chem. 29 (2014) 1–97.

[56] E. R. Johnson, I. D. Mackie, G. A. DiLabio, Dispersion interactions in density-functional theory, J. Phys. Org. Chem. 22 (2009) 1127–1135.

[57] S. Grimme, Density functional theory with london dispersion corrections, Wiley Interdisciplinary Reviews: Computational Molecular Science 1 (2011) 211–228.

[58] A. Tkatchenko, M. Scheffler, Accurate molecular van der waals interactions from ground-state electron density and free-atom reference data, Phys. Rev. Lett. 102 (2009) 073005.

[59] S. Grimme, J. Antony, S. Ehrlich, H. Krieg, A consistent and accurate ab initio parametrization of density functional dispersion correction (DFT-D) for the 94 elements H-Pu, J. Chem. Phys. 132 (2010) 154104.

[60] A. D. Becke, E. R. Johnson, Exchange-hole dipole moment and the dispersion interaction revisited, J. Chem. Phys. 127 (2007) 154108.

[61] J. Carrasco, W. Liu, A. Michaelides, A. Tkatchenko, Insight into the description of van der waals forces for benzene adsorption on transition metal (111) surfaces, J. Chem. Phys. 140 (2014) 084704.

[62] W. Liu, V. G. Ruiz, G.-X. Zhang, B. Santra, X. Ren, M. Scheffler, A. Tkatchenko, Structure and energetics of benzene adsorbed on transition-metal surfaces: density-functional theory with van der waals interactions including collective substrate response, New J. Phys. 15 (2013) 053046.

[63] K. Tonigold, A. Gross, Adsorption of small aromatic molecules on the (111) surfaces of noble metals: A density functional theory study with semiempirical corrections for dispersion effects, J. Chem. Phys. 132 (2010) 224701.

[64] W. Reckien, M. Eggers, T. Bredow, Theoretical study of the adsorption of benzene on coinage metals, Beilstein J. Org. Chem. 10 (2014) 1775–1784.

[65] H. Muñoz Galán, F. Viñes, J. Gebhardt, A. Görling, F. Illas, The contact of graphene with ni(111) surface: description by modern dispersive forces approaches, Theor Chem Acc 135 (2016) 165.

[66] M. S. Christian, A. Otero-de-la Roza, E. R. Johnson, Surface adsorption from the exchange-hole dipole moment dispersion model, J. Chem. Theory Comput. 12 (2016) 3305.

[67] W. Liu, F. Maaß, M. Willenbockel, C. Bronner, M. Schulze, S. Soubatch, F. S. Tautz, P. Tegeder, A. Tkatchenko, Quantitative prediction of molecular adsorption: Structure and binding of benzene on coinage metals, Phys.

Rev. Lett. 115 (2015) 036104.

[68] M. Dion, H. Rydberg, E. Schröder, D. C. Langreth, B. I. Lundqvist, Van der Waals density functional for general geometries, Phys. Rev. Lett. 92 (2004) 246401.

[69] T. Thonhauser, V. Cooper, S. Li, A. Puzder, P. Hyldgaard, D. Langreth, Van der waals density functional: Self-consistent potential and the nature of the van der waals bond, Phys. Rev. B 76 (2007) 125112.

[70] D. Langreth, B. I. Lundqvist, S. D. Chakarova-Käck, V. Cooper, M. Dion, P. Hyldgaard, A. Kelkkanen, J. Kleis, L. Kong, S. Li, P. G. Moses, E. Murray, A. Pudzer, H. Rydberg, E. Schröder, T. Thonhauser, A density functional for sparse matter, J. Phys.: Condens. Matter 21 (2009) 084203.

[71] K. Lee, É. D. Murray, L. Kong, B. I. Lundqvist, D. C. Langreth, Higher-accuracy van der waals density functional, Phys. Rev. B 82 (2010) 081101.

[72] H. Yildirim, T. Greber, A. Kara, Trends in adsorption characteristics of benzene on transition metal surfaces: Role of surface chemistry and van der waals interactions, J. Phys. Chem. C 117 (40) (2013) 20572–20583.

[73] Y. Zhang, W. Yang, Comment on "generalized gradient approximation made simple", Phys. Rev. Lett. 80 (1998) 890–890.

[74] V. R. Cooper, Van der Waals density functional: An appropriate exchange functional, Phys. Rev. B 81 (2010) 161104.

[75] M. S. Christian, A. O. de-la Roza, E. R. Johnson, Adsorption of graphene to nickel (111) using the exchange-hole dipole moment model, Carbon 118 (2017) 184 – 191.

[76] A. D. Becke, E. R. Johnson, Exchange-hole dipole moment and the dispersion interaction, J. Chem. Phys. 122 (2005) 154104.

[77] A. D. Becke, E. R. Johnson, Exchange-hole dipole moment and the dispersion interaction: High-order dispersion coefficients, J. Chem. Phys. 124 (2006) 014104.

[78] A. Otero-de-la Roza, E. R. Johnson, Van der waals interactions in solids using the exchange-hole dipole moment, J. Chem. Phys. 136 (2012) 174109.

[79] E. R. Johnson, The exchange-hole dipole moment dispersion model, in: A. Otero-de-la Roza, G. A. DiLabio (Eds.), Non-covalent Interactions in Quantum Chemistry and Physics, Elsevier, 2017, Ch. 5, pp. 169–194.

[80] A. Otero-de-la Roza, E. R. Johnson, Non-covalent interactions and thermochemistry using xdm-corrected hybrid and range-separated hybrid density functionals, J. Chem. Phys. 138 (2013) 054103.

[81] A. Otero-de-la Roza, E. R. Johnson, Predicting Energetics of Supramolecular Systems Using the XDM Dispersion Model, J. Chem. Theory Comput. 11 (2015) 4033.

[82] A. Otero-de-la Roza, E. R. Johnson, A benchmark for non-covalent interactions in solids, J. Chem. Phys. 137 (2012) 054103.

[83] A. Otero-de-la Roza, B. H. Cao, I. K. Price, J. E. Hein, E. R. Johnson, Density-functional theory predicts the relative solubilities of racemic and enantiopure crystals, Angew. Chem. Int. Ed. 53 (2014) 7879–7882.

[84] P. E. Blöchl, Projector augmented-wave method, Phys. Rev. B 50 (1994) 17953.

[85] P. Giannozzi, S. Baroni, et. al., Quantum espresso: a modular and open-source software project for quantum simulations of materials, J. Phys. Condens. Matter 21 (2009) 395502.

[86] A. D. Becke, On the large gradient behavior of the density functional exchange energy, J. Chem. Phys. 85 (1986) 7184.

[87] J. P. Perdew, K. Burke, M. Ernzerhof, Generalized gradient approximation made simple, Phys. Rev. Lett. 77 (1996) 3865.

[88] N. Marzari, D. Vanderbilt, A. De Vita, M. C. Payne, Thermal contraction and disordering of the Al(110) surface, Phys. Rev. Lett. 82 (1999) 3296.

[89] R. F. W. Bader, Atoms in Molecules.A Quantum Theory, Oxford University Press, Oxford, 1990.

[90] R. F. W. Bader, A quantum theory of molecular structure and its applications, Chem. Rev. 91 (5) (1991) 893.

[91] M. Yu, D. R. Trinkle, Accurate and efficient algorithm for Bader charge integration, J. Chem. Phys. 134 (2011) 064111.

[92] A. Otero-de-la Roza, E. R. Johnson, V. Luaña, Critic2: A program for real-space analysis of quantum chemical interactions in solids, Comput. Phys. Commun. 185 (2014) 1007.

[93] R. W. G. Wyckoff, Second edition, Crystal Structures 1 (1963) 7–83.

[94] T. Wiederholt, H. Brune, J. Wintterlin, R. J. Behm, G. Ertl, Formation of two-dimensional sulfide phases on Al(111): an STM study, Surf. Sci. 324 (1995) 91.

[95] L. Gao, J. R. Guest, N. P. Guisinger, Epitaxial Graphene on Cu (111), Nano Lett. (2010) 3512–3516.

[96] P. Tsipas, S. Kassavetis, D. Tsoutsou, E. Xenogiannopoulou, E. Golias, S. A. Giamini, C. Grazianetti, D. Chiappe, A. Molle, M. Fanciulli, A. Dimoulas, Evidence for graphite-like hexagonal AlN nanosheets epitaxially grown on single crystal Ag(111), Appl. Phys. Lett. 103 (25) (2013) 1.

[97] L. V. Dzemiantsova, M. Karolak, F. Lofink, A. Kubetzka, B. Sachs, K. Von Bergmann, S. Hankemeier, T. O. Wehling, R. Frömter, H. P. Oepen, A. I. Lichtenstein, R. Wiesendanger, Multiscale magnetic study of Ni(111) and graphene on Ni(111), Phys. Rev. B 84 (2011) 1.

[98] M. Enachescu, D. Schleef, D. F. Ogletree, M. Salmeron, Integration of point-contact microscopy and atomic-force microscopy: Application to characterization of graphite/Pt(111), Phys. Rev. B 60 (24) (1999) 16913.

[99] Y. S. Dedkov, M. Fonin, U. Rüdiger, C. Laubschat, Rashba effect in the graphene/Ni(111) system, Phys. Rev. Lett. 100 (2008) 1.

[100] R. Zacharia, H. Ulbricht, T. Hertel, Interlayer cohesive energy of graphite from thermal desorption of polyaromatic hydrocarbons, Phys. Rev. B 69 (2004) 1.

[101] A. Otero-de-la Roza, J. D. Mallory, E. R. Johnson, Metallophilic interactions from dispersion-corrected density-functional theory, J. Chem. Phys. 140 (2014) 18A504.

[102] M. Dion, H. Rydberg, E. Schröder, D. C. Langreth, B. I. Lundqvist, Van der waals density functional for

general geometries, Phys. Rev. Lett. 92 (2004) 246401.

[103] E. Schröder, V. R. Cooper, K. Berland, B. I. Lundqvist, P. Hyldgaard, T. Thonhauser, The vdW-DF family of nonlocal exchange-correlation functionals, in: A. Otero-de-la Roza, G. A. DiLabio (Eds.), Non-covalent Interactions in Quantum Chemistry and Physics, Elsevier, 2017, Ch. 8, pp. 241–274.

[104] J. Cho, L. Gao, J. Tian, H. Cao, W. Wu, Q. Yu, E. N. Yitamben, B. Fisher, J. R. Guest, Y. P. Chen, N. P. Guisinger, Atomic-scale investigation of graphene grown on Cu foil and the effects of thermal annealing, ACS Nano 5 (2011) 3607–3613.

[105] N. R. Wilson, A. J. Marsden, M. Saghir, C. J. Bromley, R. Schaub, G. Costantini, T. W. White, C. Partridge, A. Barinov, P. Dudin, A. M. Sanchez, J. J. Mudd, M. Walker, G. R. Bell, Weak mismatch epitaxy and structural Feedback in graphene growth on copper foil, Nano Res. 6 (2013) 99–112.